INORGANIC CHEMISTRY FRONTIERS

RESEARCH ARTICLE

View Article Online
View Journal | View Issue

Cite this: *Inorg. Chem. Front.*, 2024, **11**, 3607

Temperature-dependent self-trapped models regulating energy transfer in rare earth double perovskites *via* $5s^2$ electron doping†

Chujun Tan, Shuai Zhang, Haiyan Wang, Jiandong Yao, Hongbang Liu,* Bingsuo Zou * and Ruosheng Zeng *

Due to their environmental friendliness, structural plasticity, and tunable emission, lead-free halide double perovskites offer a broad spectrum of applications in light-emitting diode (LED), photodetectors, infrared imaging, and temperature sensing. Herein, we synthesized rare earth-based Cs_2NaYCl_6 double perovskites using a solvothermal method, and Sb^{3+}/Sm^{3+} co-doping can effectively modulate the luminescence by adjusting the band gap structure and channels of energy transfer. With the Sm^{3+}-feeding concentration increasing, the emission could be adjusted from blue to white, attributed to an effective energy transfer from the self-trapped state to Sm^{3+}. Temperature-dependent photoluminescence spectra indicate that the double self-trapped exciton emission at low temperatures originated from two minima in the excited state of $^3P_1$. The relative sensitivity of the optical temperature sensor reached 1.08% K^{-1}, which was better than that of other rare earth perovskites. The LED device based on Sb^{3+}/Sm^{3+} co-doped Cs_2NaYCl_6@polymethylmethacrylate displays a chromaticity coordinate of (0.29, 0.28), a color rendering index of 87, and the correlated color temperature of 10 986 K. Our work explores an in-depth understanding of energy transfer in double self-trapped states and provides new material for advanced applications.

Received 13th March 2024,
Accepted 6th May 2024

DOI: 10.1039/d4qi00649f

rsc.li/frontiers-inorganic

1. Introduction

Lead-based halide perovskites (A = $MA^+/FA^+/Cs^+$ and X = $Cl^-/Br^-/I^-$), typically characterized by $APbX_3$, have garnered significant attention due to their excellent photovoltaic properties, including high light absorption coefficients, low defect densities, and large electron sizes.[1–3] Based on these advantages, lead-based perovskites have been found to have broad applications in many fields, such as light emitting diodes (LEDs) and[4,5] X-ray detectors.[6] The disadvantages of a low stability and environmental unfriendliness are also accompanied by lead-based perovskites.[7] However, environmentally friendly cation substitution is an effective strategy to overcome the toxicity of Pb^{2+} ions. Replacing two Pb^{2+} cations as B^+ and B^{3+} sites in halide double perovskites with the formula $A_2B^+B^{3+}X_6$ (*e.g.* $Cs_2NaInCl_6$)[8] is a universal strategy.[9–15] However, indirect bandgap or parity prohibited transition cause a weak photoluminescence (PL) in pristine lead-free perovskites. Doping with metal ions or alloying can alter the bandgap or disrupt the symmetry of double perovskites, breaking forbidden transitions and thereby enhancing their optical properties. By introducing Na^+ and Bi^{3+} into the $Cs_2AgInCl_6$ host, Tang's group broke the inversion-symmetry-induced parity-forbidden transition and reduced the electronic dimensionality of the semiconductor, thus achieving an effective white light emission.[16] By introducing Sb^{3+} into the $Cs_2NaInCl_6$ host, our group effectively regulated the density of states (DOS) and significantly enhanced the PL quantum yield (QY) of the self-trapped exciton (STE) (up to 75.89%).[8] However, aforementioned studies only achieved a single luminescence mode. It is widely recognized that doping with rare earth elements is an effective method for tuning luminescent color.[17–22] Rare earth ions typically exhibit a wide emission range from ultraviolet (UV) to infrared due to their rich ($4f^n$) electronic configurations, along with long PL lifetimes and excellent optical stability.[23–26] Xia's group reported on Bi^{3+}:$Cs_2Ag(In_{1-x}Tb_x)Cl_6$ halide perovskites,[27] which modulated luminescence from green to orange. However, the tuning range of luminescence did not extend to cover the entire spectrum. Tang *et al.* confirmed the existence of an energy transfer from a STE to a rare earth in Ho^{3+}:Cs_2(Na, Ag)$InCl_6$ and fabricated white LED.[28] Zhu *et al.* obtained white light emission by combining $CsPbBr_3$ NCs and $Cs_2Ag_{1-x}K_xIn_{0.125}Bi_{0.875}Cl_6$ double perovskites.[29] The stability of double perovskites is significantly improved through K^+ ion alloying. However, the lower PLQY of 15.96% limited broader application. Overall, abovementioned

State Key Laboratory of Featured Metal Materials and Life-cycle Safety for Composite Structures, School of Physical Science and Technology, Guangxi University, Nanning 530004, China. E-mail: liuhb@gxu.edu.cn, zoubs@gxu.edu.cn, zengrsh@guet.edu.cn

† Electronic supplementary information (ESI) available. See DOI: https://doi.org/10.1039/d4qi00649f

works only focus on LED applications and do not realize the multi-functional application of phosphors. Furthermore, the luminescence of all these works originates from the single self-trapped state and how to regulate the energy transfer process is not understood in depth.

In this work, Sb^{3+}/Sm^{3+} co-doped Cs_2NaYCl_6 were synthesized by a solvent-thermal method, resulting in the emission color transitioning steadily from blue to warm white with increasing Sm^{3+} feeding concentration. When a 2% Sm^{3+} precursor is the feed, the PLQY is as high as 68%. We propose a model to explain physical processes associated with energy transfer from the STE to the Sm^{3+} energy level. The single STE emission was observed at a higher temperature (up to 260 K), but the excited state $^3P_1$ was split into two minima and resulted in a double STE emission at a lower temperature (below 260 K). $5s^2$ electron doping (Sb^{3+}-doping) facilitates the energy transfer efficiency. Furthermore, we attempted multi-functional applications of the phosphors. At room temperature, the LED device exhibits chromaticity coordinates (CIE) of (0.28, 0.29), a color rendering index (CRI) of 87 and the correlated color temperature (CCT) of 10 986 K, and the efficient infrared emission (400–1250 nm) is suitable for advanced infrared imaging. Further, the non-contact optical thermometry of Sb^{3+}/Sm^{3+} co-doped Cs_2NaYCl_6 has demonstrated that absolute and relative sensitivities can reach 0.14% K^{-1} and 1.08% K^{-1}, respectively. Our work provides new physical insights into regulating energy transfer and references for the rational design of functional materials.

2. Results and discussion

Pristine and Sb^{3+}/Sm^{3+} co-doped Cs_2NaYCl_6 are of a highly symmetric three-dimensional cubic structure belonging to the $Fm\bar{3}m$ space group. Cs_2NaYCl_6 consists of alternately arranged $[NaCl_6]^{5-}$ and $[YCl_6]^{3-}$ octahedra (Fig. 1a). The powder X-ray diffraction (PXRD) analysis reveals that the introduction of Sb^{3+} ions causes a shift in diffraction peaks towards higher angles, as seen in Fig. 1b. This shift is due to the smaller ionic radius of Sb^{3+} (76.0 pm) compared to that of Y^{3+} (90.0 pm), which results in the contraction of the lattice. Conversely, an increase in the Sm^{3+}-feeding concentration leads to the diffraction peaks shifting towards lower angles. This shift originates from the substitution of Sb^{3+}/Sm^{3+} ions for Y^{3+} ions due to the larger ionic radius of Sm^{3+} (95.8 pm) compared to that of Y^{3+} (90.0 pm), and lattice expansion dominates a further shift. Due to the low doping content, no large change in lattice parameters was observed. The impurity peaks at 31.7° and 45.6° were from NaCl; however, a slight excess of NaCl is necessary for synthesizing samples with high yields. The X-ray photoelectron spectra (XPS) of pristine and doped perovskites show that the peaks at 160.4 and 158.5 eV are attributed to the Y 3d orbital (Fig. 1c) with no significant deviations. Fig. 1d shows the peaks of the Sb 3d orbital of Sb^{3+}/Sm^{3+} co-doped Cs_2NaYCl_6, which are located at 535.9 and 531.9 eV. Moreover, Fig. 1e shows the peak of the Sb 3d orbital, which is located at 1088.4 eV. The XPS spectra of Cs, Na and Cl of pristine and Sb^{3+}/Sm^{3+} co-doped Cs_2NaYCl_6 samples in Fig. S1† indicate that no striking deviations in binding energies are observed between pristine and Sb^{3+}/Sm^{3+} co-doped Cs_2NaYCl_6 perovskites, which is attributed to the strong electronegativity of the rare earth ions. As shown in Fig. 1f, a scanning electron microscopy (SEM) image shows that the Sb^{3+}/Sm^{3+} co-doped Cs_2NaYCl_6 perovskites are of micrometer scale. Furthermore, the energy-dispersive X-ray spectroscopy (EDS) mapping indicated Cs, Na, Y, Cl, Sb and Sm elements were uniformly distributed in the crystal.

To further investigate the optical properties of Sb^{3+}/Sm^{3+} co-doped Cs_2NaYCl_6, PL, PL excitation (PLE), time-resolved PL (TRPL), and absorption spectroscopy have been performed. As shown in Fig. S2,† the absorption spectrum of pristine Cs_2NaYCl_6 shows a strong absorption at 310 nm and two weak absorption bands at 355 and 402 nm. After Sb^{3+} doping, the whole absorption band is enhanced, and a new absorption band appears at 260 and 300 nm originating from the $^1S_0 \rightarrow {}^3P_1$ of Sb^{3+}. The absorption spectra of Sm^{3+}-doped samples are basically the same as those of undoped samples, which indicate that the introduction of Sm^{3+} does not contribute to the absorption, or absorption peaks overlap. As shown in Fig. S3a,† under 268 nm excitation, the double perovskites exhibit a broadband blue emission centered at 465 nm with a Stokes shift of 1.96 eV. After Sb^{3+} doping, the PL intensity of Sb^{3+}:Cs_2NaYCl_6 is more than 10 times that of the pristine sample, with a Stokes shift of 0.93 eV. A large Stokes shift is a distinctive feature of STE emission. Simultaneously, the PL intensity of Sb^{3+}/Sm^{3+} co-doped Cs_2NaYCl_6 is significantly enhanced by Sb^{3+} doping, achieving more than 30 times that of Sm^{3+}:Cs_2NaYCl_6, as illustrated in Fig. S3b.† As a bridge of energy transfer, $5s^2$ dopants can more effectively transfer excited electrons from the excited state to the energy level of the rare earth ions. This is because STE emission possesses a wide excitation region and large absorption strength, which can overcome the weak absorption of the f–f transition through the efficient energy transfer. These indicate that the doping of Sb^{3+} greatly improves the luminescence efficiency of the samples. At room temperature, under 345 nm excitation, the Sb^{3+}/Sm^{3+} co-doped Cs_2NaYCl_6 double perovskites exhibits STE emission centered at 465 nm (Fig. 2a), where the visible (VIS) emission at 565, 603, 651 and 712 nm is from the $^4G_{5/2} \rightarrow {}^6H_{J=(5/2,\ 7/2,\ 9/2,\ 11/2)}$ energy level transitions of Sm^{3+}, and the near-infrared (NIR) emission at 941, 951, 1026 and 1170 nm is from the $^4G_{5/2} \rightarrow {}^6F_{K=(9/2,\ 7/2,\ 5/2,\ 3/2)}$ energy level transitions of Sm^{3+}.[30] By normalizing the intensity of STE emission at 465 nm, the intensity of the rare earth emission from Sm^{3+} is gradually enhanced with increasing Sm^{3+}-feeding concentration. Three excitation peaks at 285, 320, and 345 nm of the Sb^{3+}/Sm^{3+} co-doped Cs_2NaYCl_6 double perovskites at different emissions can be observed in Fig. 2b. The peak at 285 nm is attributed to the transition from the singlet $^1S_0$ to $^1P_1$ of Sb^{3+}, while excitation peaks at 320 and 345 nm correspond to the transitions from the ground state $^1S_0$ to triplet $^3P_1$. The excitation peak at 410 nm originates from the $^6H_{5/2} \rightarrow {}^4F_{7/2}$ tran-

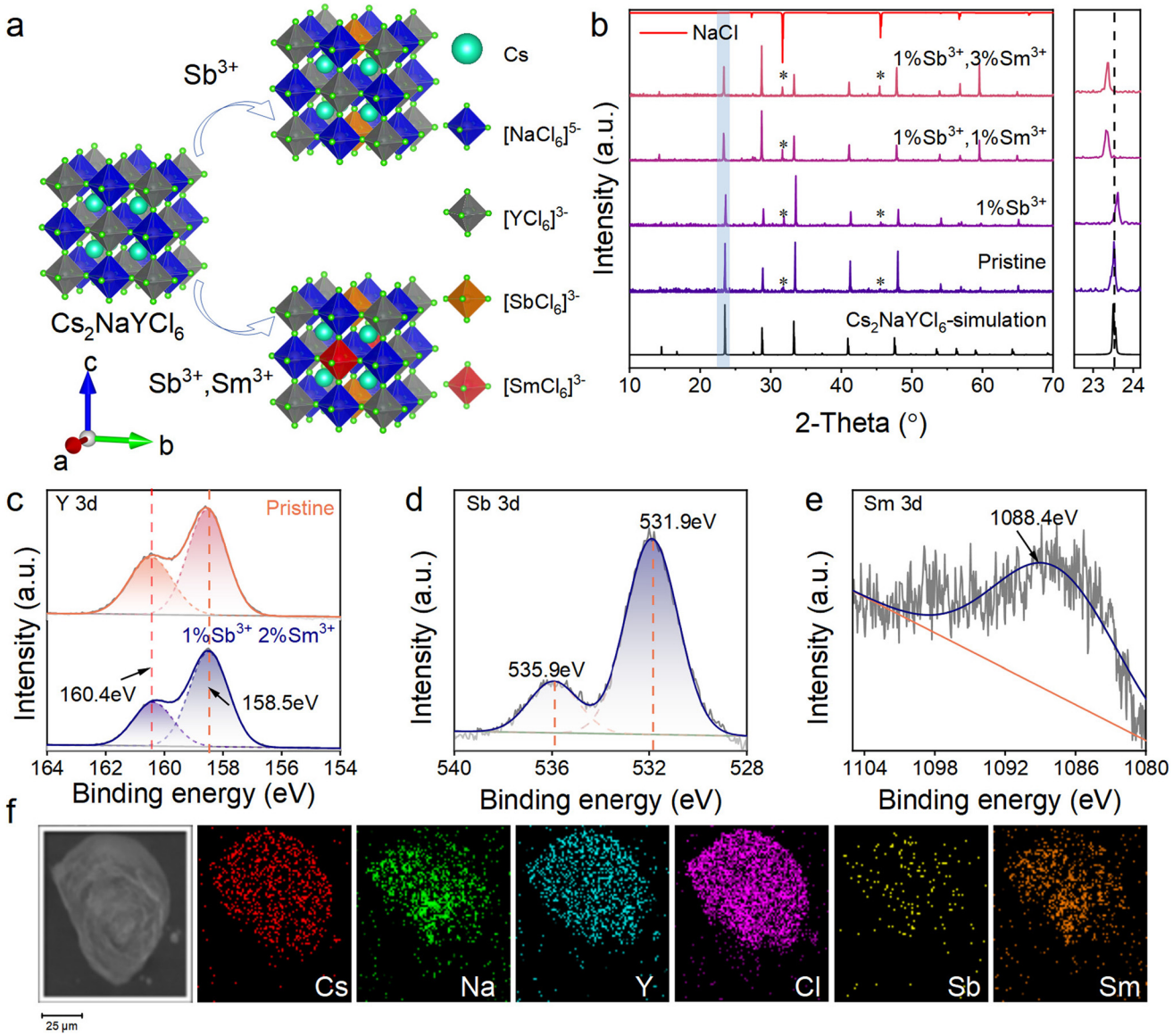

Fig. 1 (a) Crystal structures of pristine Cs_2NaYCl_6, Sb^{3+}:Cs_2NaYCl_6 and 1% Sb^{3+}, 2% Sm^{3+} co-doped Cs_2NaYCl_6. (b) PXRD patterns of pristine and doped Cs_2NaYCl_6 double perovskites. High-resolution XPS spectra of Y 3d (c), Sb 3d (d) and Sm 3d (e). (f) SEM image and element mapping of 1% Sb^{3+}, 2% Sm^{3+} co-doped Cs_2NaYCl_6 double perovskites.

sition of the Sm^{3+} ion.[31] The profiles of the PLE in NIR emission in Fig. 2c is similar to that in Fig. 2b, indicating that almost all NIR emissions are from the energy transfer from Sb^{3+} to Sm^{3+}, and only a very small portion comes from $^6H_{5/2} \rightarrow {}^4F_{7/2}$ of the Sm^{3+} ions. Fig. 2d shows PL spectra normalized at 465 nm under different excitations. As the excitation wavelength increases, the emission intensity of Sm^{3+} emission relative to STE emission gradually increases, which indicates that Sb^{3+}/Sm^{3+} co-doped Cs_2NaYCl_6 has an excitation wavelength dependence.[32] The integral area ratio $S_{550-750}/S_{400-550}$ of STE emission to Sm^{3+} emission is shown in Fig. 2e, which is positively correlated with the Sm^{3+}-feeding concentration, indicating the promoted energy transfer from $^3P_1$ of Sb^{3+} to $^4D_{5/2}$ of Sm^{3+}. CIE coordinates that correspond to the PL spectra at varying Sm^{3+}-feeding concentrations are depicted in Fig. S4.† As the Sm^{3+}-feeding concentration increases, the luminescence gradually shifts from blue to white. The initial CIE coordinate is (0.19, 0.21), and the final CIE coordinate is (0.36, 0.32). The PLQY reaches a maximum of 68% at a 2% Sm^{3+}-feeding concentration and further gradually decreases with further increasing the Sm^{3+}-feeding concentration (Fig. S5†). Broad-band STE emission is usually accompanied by a large Stokes shift, with barely any self-absorption in the PL process. This is also the reason why the sample has a higher PLQY. Fig. 2f demonstrates that the integral area ratio of Sm^{3+} emission to STE emission increases with increasing excitation wavelength. The PL decay spectra of Sb^{3+}/Sm^{3+} co-doped Cs_2NaYCl_6 at 465 nm under a 345 nm excitation are shown in Fig. 2g, and specific values are expressed in

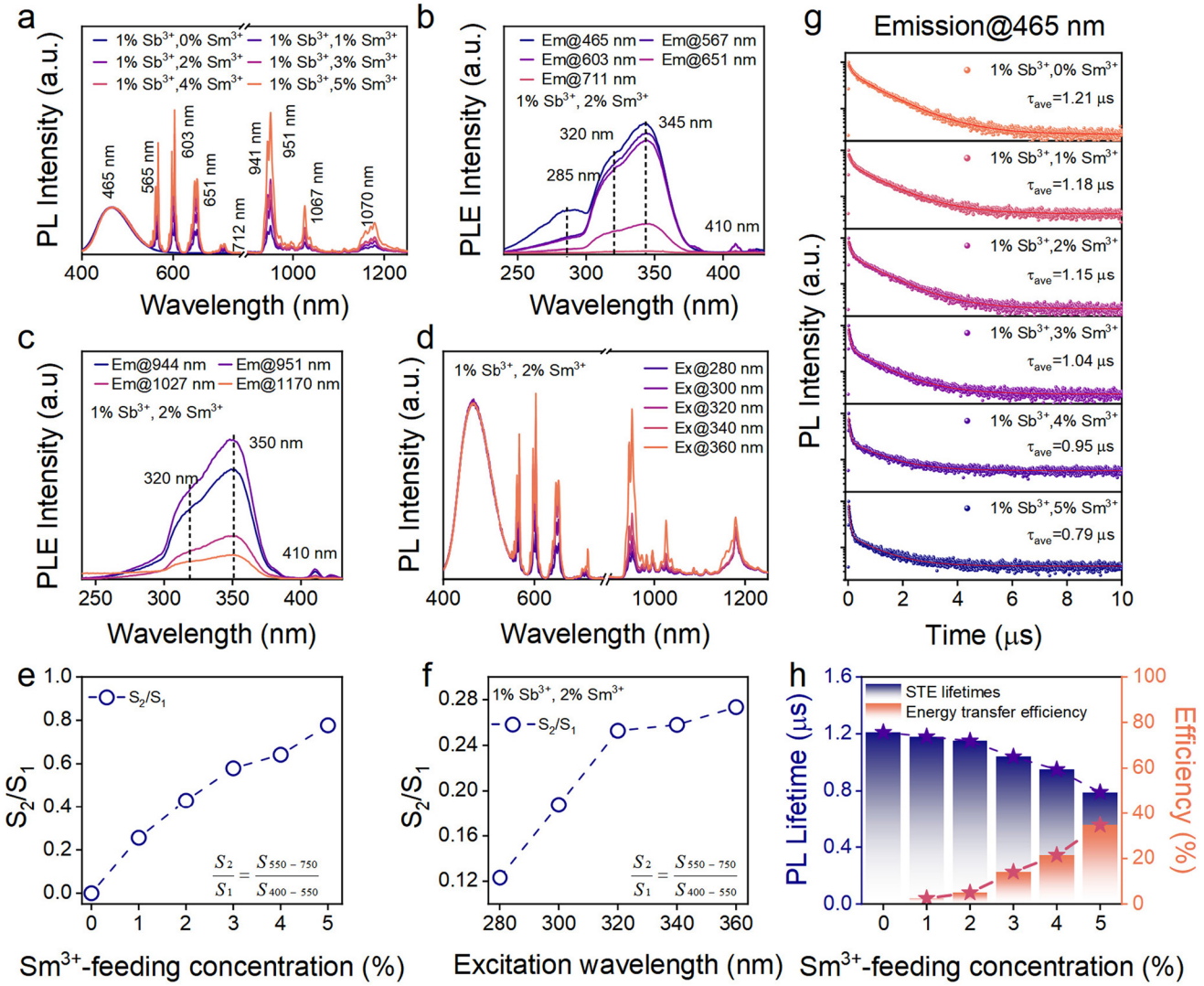

Fig. 2 (a) Normalized PL spectra of the 1% Sb^{3+}, *x*% Sm^{3+} co-doped Cs_2NaYCl_6 (*x* = 1, 2, 3, 4 and 5) double perovskites with different Sm^{3+}-feeding concentrations under 345 nm excitation. (b) PLE spectra of the 1% Sb^{3+}, 2% Sm^{3+} co-doped Cs_2NaYCl_6 double perovskites at different emissions. (c) PLE spectra of the 1% Sb^{3+}, 2% Sm^{3+} co-doped Cs_2NaYCl_6 double perovskites under different NIR emissions. (d) Normalized PL spectra of the 1% Sb^{3+}, 2% Sm^{3+} co-doped Cs_2NaYCl_6 double perovskites under different excitations. (e) Integral area ratio $S_{550-750}/S_{400-550}$ of the STE emission to Sm^{3+} emission in 1% Sb^{3+}, *x*% Sm^{3+} co-doped Cs_2NaYCl_6 (*x* = 1, 2, 3, 4 and 5) crystals with different Sm^{3+}-feeding concentrations. (f) Integral area ratio of $S_{550-750}/S_{400-550}$ of the 1% Sb^{3+}, 2% Sm^{3+} co-doped Cs_2NaYCl_6 double perovskites under different excitations. (g) PL decay curves of the 1% Sb^{3+}, *x*% Sm^{3+} co-doped Cs_2NaYCl_6 (*x* = 1, 2, 3, 4 and 5) double perovskites monitored at 465 nm. (h) PL lifetimes and energy transfer efficiency of the 1% Sb^{3+}, *x*% Sm^{3+} co-doped Cs_2NaYCl_6 (*x* = 1, 2, 3, 4 and 5) double perovskites with different Sm^{3+}-feeding concentrations.

Table S1.† The PL lifetime at 465 nm decreases from 1.21 to 0.79 μs with increasing Sm^{3+}-feeding concentration. All the emissions exhibit microsecond lifetimes corresponding to the $^1S_0 \rightarrow {}^3P_1$ transition of Sb^{3+}. This changing trend indicates an efficient energy transfer from the STE to Sm^{3+} exists (Fig. 2h). The energy transfer efficiency of the STE to Sm^{3+} can be expressed by the following eqn (1):[27,33]

$$\eta = 1 - \frac{\tau_x}{\tau_0}, \quad (1)$$

where τ_0 and τ_x are the PL lifetimes of STE emission without and with Sm^{3+} doping. The energy transfer efficiencies with different Sm^{3+}-feeding concentrations are 2.48% (Sm^{3+}:1%), 4.96% (Sm^{3+}:2%), 14.05% (Sm^{3+}:3%), 21.49% (Sm^{3+}:4%), and 34.71% (Sm^{3+}:5%). These indicate that the energy transfer efficiency increases with increasing Sm^{3+}-feeding concentration. The PL lifetimes of Sb^{3+}/Sm^{3+} co-doped Cs_2NaYCl_6 at 651 and 951 nm decreases with Sm^{3+}-feeding concentration and are of the millisecond scale (Fig. S6†), suggesting concentration quenching due to the increased Sm^{3+}-feeding concentration. A schematic diagram of the photophysical mechanism of the Sb^{3+}/Sm^{3+} co-doped Cs_2NaYCl_6 double perovskites at a high temperature is shown in Fig. S7.† The electrons transitioned from the ground state (GS) to the free electron (FE)

state under ultraviolet excitation. Then, through Intersystem Crossing (ISC), the excited electrons arrive at the $^3P_1$ energy level of Sb^{3+}, *via* the $^3P_1 \rightarrow {}^1S_0$ transition producing STE emission and part of the energy transmitted to the excitation level $^4G_{5/2}$ of Sm^{3+}, further generating the corresponding Sm^{3+} emission by radiative recombination.

To gain more understanding about the electron-optical phonon coupling of 1% Sb^{3+}, 2% Sm^{3+} co-doped Cs_2NaYCl_6, temperature-dependent PL spectroscopy was utilized to explore the photophysical process. The PL spectra at 140 and 300 K are shown in Fig. 3a. The PL spectra shows a double STE emission at 140 K and only a single STE emission at 300 K. The emis-

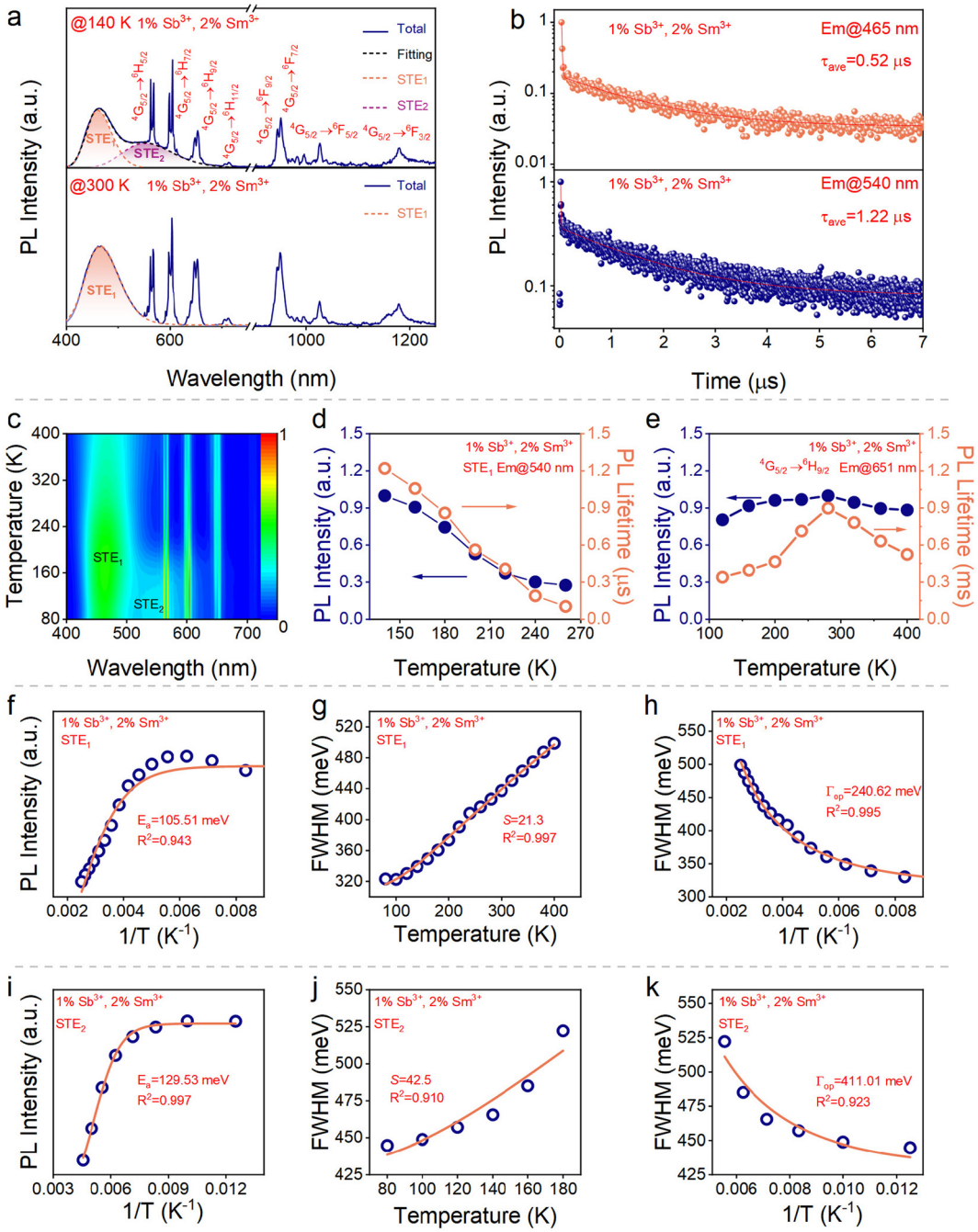

Fig. 3 (a) PL spectra of 1% Sb^{3+}, 2% Sm^{3+} co-doped Cs_2NaYCl_6 at 140 and 300 K. (b) PL lifetime of 1% Sb^{3+}, 2% Sm^{3+} co-doped Cs_2NaYCl_6 at 140 and 300 K. (c) Pseudo-color map from temperature-dependent PL spectra of 1% Sb^{3+}, 2% Sm^{3+} co-doped Cs_2NaYCl_6. The evolutions of the PL lifetime and intensity at 540 (d) and 651 nm (e) with temperature. The fitted exciton activation energy E_a (f), Huang–Rhys factor S (g) and electron-optical phonon coupling (h) of STE_1. The fitted exciton activation energy E_a (i), Huang-Rhys factor S (j) and electron-optical phonon coupling (k) of STE_2.

sion centered at 465 nm is defined as STE_1, and the emission centered at 550 nm is defined as STE_2. Comparing Sb^{3+}/Sm^{3+} co-doped Cs_2NaYCl_6 with similar Sb-doped systems,[34] there are two possible explanations for the double STE emission at low temperatures. One is due to the bimodality that arises from the dynamical Jahn–Teller coupling of the orbital triplet state $^3P_1$ to two minima.[35] The excited state shows two minima, which result in two different emission bands. Another reason is that the single state $^1P_1 \rightarrow {}^1S_0$ transition and triple state $^3P_1 \rightarrow {}^1S_0$ transition co-exist together. To study the source of the double STE emission at low temperatures, the lifetimes of STE_1 and STE_2 emissions were monitored separately at 140 K (Fig. 3b). The PL lifetimes of 0.52 and 1.22 μs for high-energy and low-energy emissions are obtained (Fig. 3b), respectively. The PL lifetimes of both STE emissions are in the microsecond scale. Sb^{3+} is characterized by a typical electron configuration of $5s^2$,[36] exhibiting STE emission with nanosecond lifetimes resulting from the transition of $^1P_1$ to $^1S_0$ [37] and microsecond lifetimes arising from the transition of $^3P_1$ to $^1S_0$. Therefore, the STE_1 and STE_2 emissions of Sb^{3+}/Sm^{3+} co-doped Cs_2NaYCl_6 belong to the triplet state emission. Temperature-dependent PL spectra and pseudo-color maps are shown in Fig. 3c and S8,† and double STE emission can be clearly detected from 80 to 260 K and Sm^{3+} emission positions are largely independent of temperature. This is because the f–f transition of rare earths is not easily affected by temperature, and the two minima of the $^3P_1$ orbital of Sb^{3+} result in a double STE emission at low temperatures. Fig. 3d shows the variation of PL lifetime and intensity at 540 nm from 140 to 260 K, and both show a decreasing trend with increasing temperatures due to thermal quenching. As shown in Fig. S9,† the PL intensity at 465 nm increases gradually with temperature. This is attributed to the electrons gaining more energy and so tend to a higher energy radiative transition with increasing temperature. Fig. 3e shows the variation of PL lifetime and intensity at 651 nm from 120 to 400 K. PL intensity and lifetime increase from 120 to 280 K, which is attributed to the weakening of phonon scattering and reduction of defects more favorable to radiative recombination at low temperature. While PL intensity and lifetime show a decreasing trend from 280 to 400 K, which is attributed to thermal quenching at the high temperature. As shown in Fig. 3f and i, STE_1 and STE_2 were fitted using eqn (2), respectively.[38,39]

$$I(t) = I_0/(1 + Ae^{-E_a/TK_B}), \quad (2)$$

where $I(t)$ is the integrated PL intensity at the experimental temperature, E_a is the exciton activation energy. I_0 is the integrated intensity at 0 K, K_B is the Boltzmann constant, and T is the temperature. For STE_1 and STE_2, exciton activation energies are 105.51 and 129.53 meV, respectively. These values significantly exceed the thermal activation energy of 26 meV at room temperature. This suggests that the highly localized STE are stable.

Huang Rhys factor S is obtained by fitting the full width at half-maximum (FWHM) and temperature (T) using the following eqn (3):[16,40]

$$\mathrm{FWHM}(T) = 2.36\sqrt{S}\hbar\omega_{\mathrm{phonon}}\sqrt{\coth\frac{\hbar\omega_{\mathrm{phonon}}}{2K_BT}}, \quad (3)$$

where $\hbar\omega_{\mathrm{phonon}}$ is the phonon frequency, K_B is the Boltzmann constant, and T is the thermodynamic temperature. The value of S represents the electron–phonon coupling parameter, directly influencing the degree of lattice distortion and manifesting in a significant Stokes shift.[41,42] STE_2 exhibits a greater Stokes shift than that of STE_1, as depicted in Fig. S10.† S values for STE_1 and STE_2 are 21.3 and 42.5, respectively, suggesting that STE_2 experiences a greater lattice distortion (Fig. 3g and j).

The electron-optical phonon coupling energy Γ_{op} was fitted using the following eqn (4):[43]

$$\Gamma(T) = \Gamma_0 + \Gamma_{op}/(e^{\hbar\omega_{op}/K_BT} - 1), \quad (4)$$

where Γ_0 represents the intrinsic line width at 0 K, and $\hbar\omega_{op}$ denotes the longitudinal optical phonon energy. According to eqn (4), the values of Γ_{op} for STE_1 and STE_2 are determined as 240.62 and 411.01 meV, respectively (Fig. 3h and k). These Γ_{op} values indicate a substantial interaction between electrons and phonons, as well as the Jahn–Teller effect contributing to the lattice transient STE_2 having a greater electro-phonon coupling energy, implying stronger Jahn–Teller effect and lattice distortions, which match its larger S value.[44] Fig. S11† depicts a schematic illustration of the physical mechanism of Sb^{3+}/Sm^{3+} co-doped Cs_2NaYCl_6 at low temperatures. This is somewhat different from the mechanism diagram at high temperatures (Fig. S7†). When the excited electrons arrive, the $^3P_1$ energy level of Sb^{3+} and two minima in the $^3P_1$ energy level result in a double STE emission at low temperatures. Meanwhile, benefiting from the energy-transfer channel from STE to Ln^{3+}, part of the energy can be transferred to the Sm^{3+} ions to emit multicolor.

To get a better knowledge of the electrical structure and luminous characteristics of Cs_2NaYCl_6 and Sb^{3+}/Sm^{3+} co-doped Cs_2NaYCl_6, we performed density functional theory (DFT) calculations on pristine and Sb^{3+}/Sm^{3+} co-doped Cs_2NaYCl_6 structures. Because of the covalent states of Sb^{3+}/Sm^{3+} and Y^{3+}, a $[SbCl_6]^{3-}$ and $[SmCl_6]^{3-}$ octahedron is used to replace the $[YCl_6]^{3-}$ octahedron. It is found that pristine Cs_2NaYCl_6 exhibits a flat energy band structure with a direct band gap of 5.01 eV (Fig. 4a). After Sb^{3+} doping, the emergence of a new energy level results in a narrower bandgap of 3.75 eV (Fig. 4b). Furthermore, both structures have very flat energy bands with limited dispersion, indicating a large effective mass and confined properties for electrons and holes, which promotes the creation of highly localized electron distributions. The calculated DOS reveals that the valence band maximum (VBM) of Cs_2NaYCl_6 primarily comprises the Cl 3p state, while the conduction band minimum (CBM) is composed of Y 4d and Cl 3p states, as illustrated in Fig. 4c. The

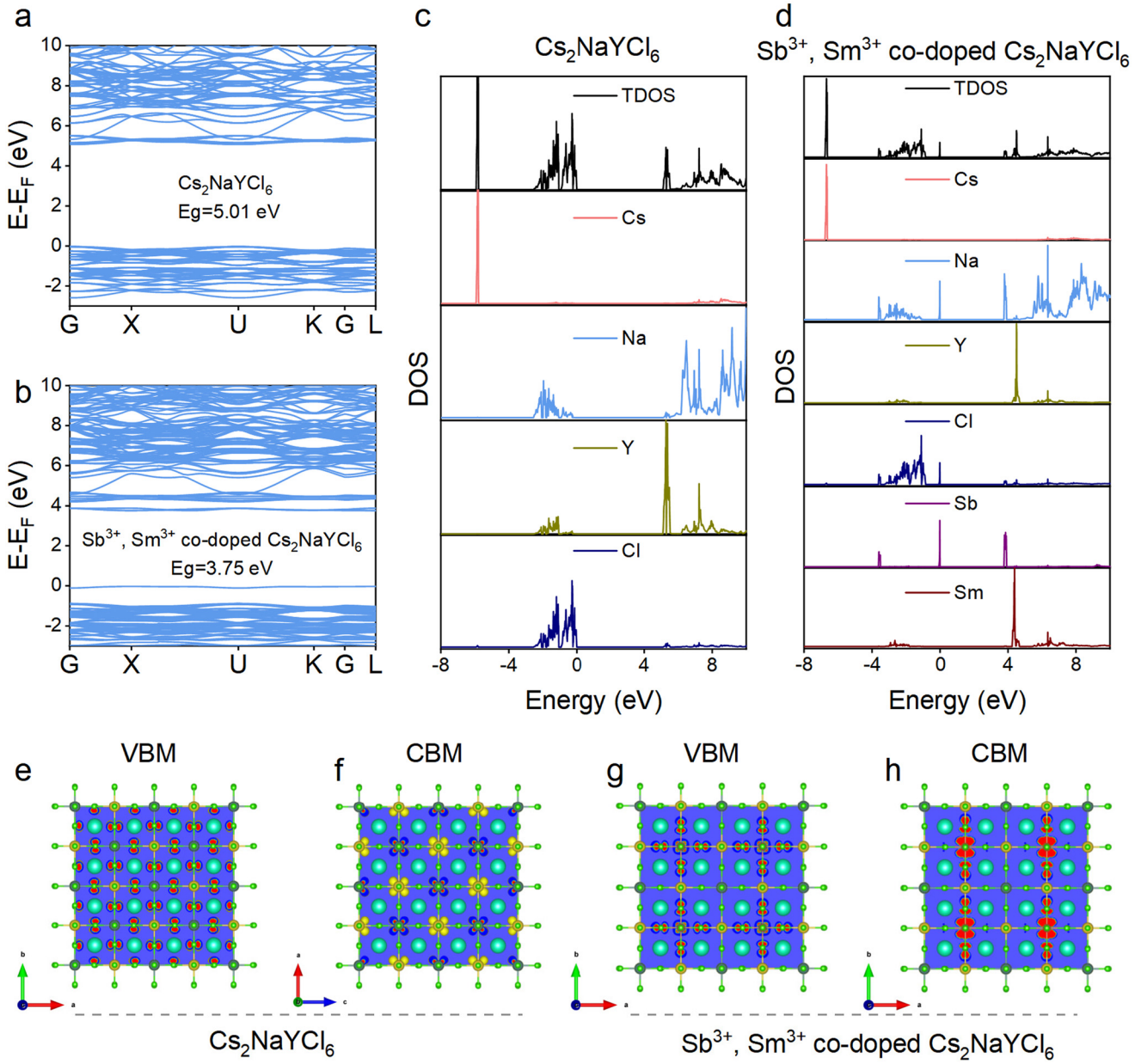

Fig. 4 Calculated electronic band structures of Cs_2NaYCl_6 (a) and Sb^{3+}/Sm^{3+} co-doped Cs_2NaYCl_6 (b). DOS of Cs_2NaYCl_6 (c) and Sb^{3+}/Sm^{3+} co-doped Cs_2NaYCl_6 (d). Charge densities of Cs_2NaYCl_6 (e and f) and Sb^{3+}/Sm^{3+} co-doped Cs_2NaYCl_6 (g and h).

VBM of Sb^{3+}/Sm^{3+} co-doped Cs_2NaYCl_6 consisted of Sb 5s and Cl 3p states, and the CBM consisted of the Sb 5p state (Fig. 4d). Dopant s-electrons mainly contribute near the band edges of the host. So, the s-electron dopants (Sb^{3+}) act as sensitizers and emitters. The charge density distribution of pristine Cs_2NaYCl_6 reveals that the charge of the VBM is primarily concentrated around $[YCl_6]^{3-}$ octahedra, as depicted in Fig. 4e. Conversely, the charge of the CBM is concentrated around Cl (Fig. 4f). The charge density distribution of Sb^{3+}/Sm^{3+} co-doped Cs_2NaYCl_6 reveals that the charge of the VBM is primarily concentrated around the $[YCl_6]^{3-}$ octahedra (Fig. 4g). The charge of the CBM is concentrated around $[SbCl_6]^{3-}$ octahedra (Fig. 4h).

To explore the potential applications of the Sb^{3+}/Sm^{3+} co-doped Cs_2NaYCl_6 double perovskites, the stability of the samples in the environment was initially investigated. Fig. S12† presents a comparison of the XRD and PL spectra of the sample after one month with those of the fresh sample, demonstrating a good environmental stability at room temperature and a high humidity of 70%. Our samples were placed in a relatively high humidity environment (70%) for one month. From the XRD pattern, a NaCl impurity was observed, and the main diffraction peaks of the samples did not obviously change, which indicated that the samples were of high humidity stability and good humidity resistance. Fig. 5a demonstrates that the LED device, emitting cool white light,

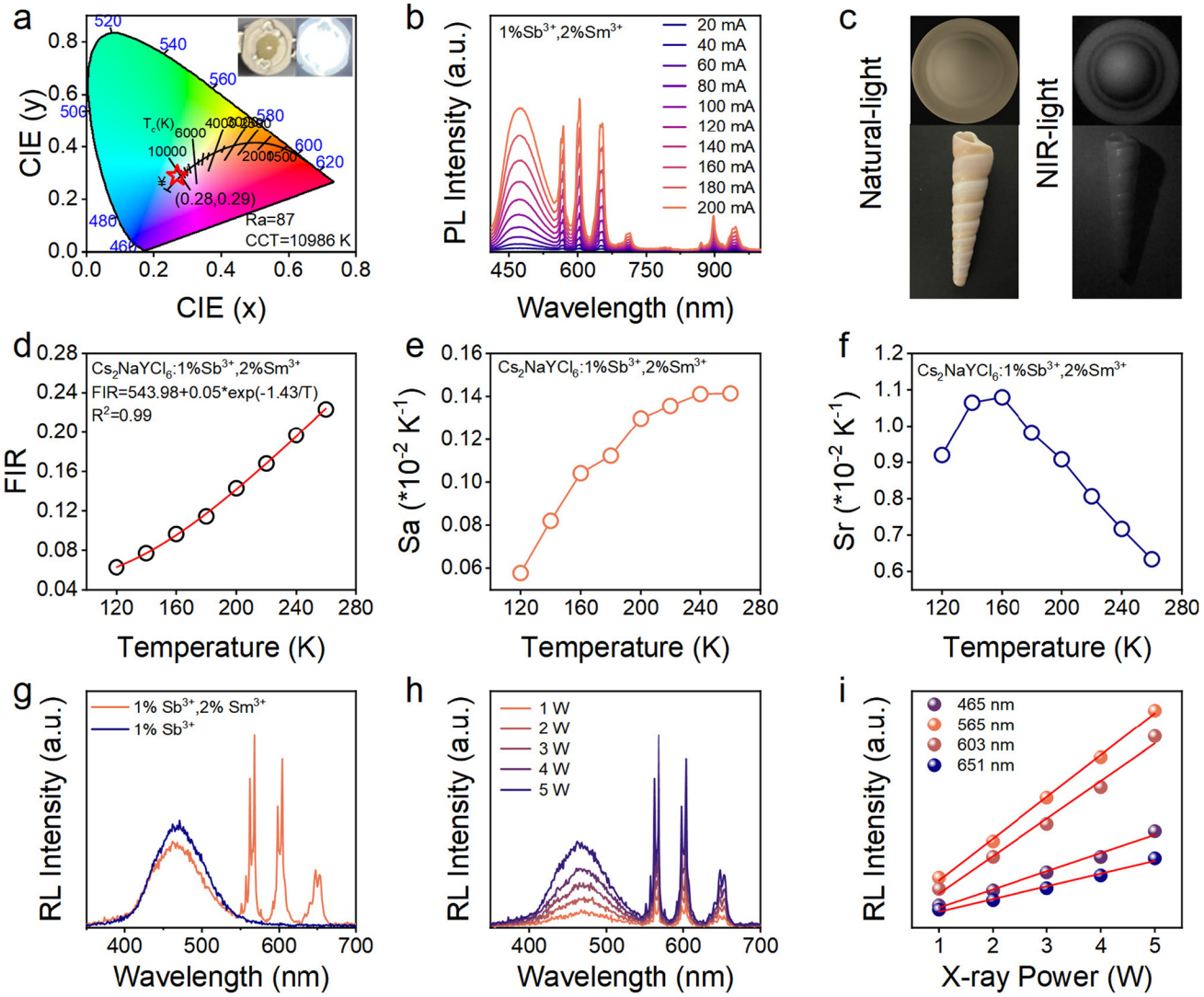

Fig. 5 (a) CIE of 1% Sb^{3+}, 2% Sm^{3+} co-doped Cs_2NaYCl_6. (b) PL spectra of the 1% Sb^{3+}, 2% Sm^{3+} co-doped Cs_2NaYCl_6 double perovskites under different currents. (c) Photos of a coffee cup lid and conch under natural and NIR light, respectively. FIR (d), S_a (e) and S_r (f) as functions of temperature. (g) RL spectra of the 1% Sb^{3+}, 2% Sm^{3+} co-doped Cs_2NaYCl_6 double perovskites. (h) Variable power X-ray spectrum. (i) RL intensity variation with power at different emissions.

that was fabricated by integrating the Sb^{3+}/Sm^{3+} co-doped Cs_2NaYCl_6 double perovskites with polymethylmethacrylate (PMMA) on a 365 nm UV chip, achieving a CRI of up to 87. The LED device exhibits a CIE of (0.28, 0.29) and a CCT of 10 986 K. Furthermore, the prepared LED lamp exhibited an excellent spectral stability across various currents ranging from 20 to 200 mA, as illustrated in Fig. 5b. Different imaging photographs of a conch and coffee cap under natural light irradiation and NIR light irradiation are depicted in Fig. 5c. Furthermore, the observation of different energy level transitions of Sm^{3+} with varying temperature sensitivities prompted us to explore the utilization of Sb^{3+}/Sm^{3+} co-doped Cs_2NaYCl_6 for temperature sensing. As shown in Fig. S13,† we observe a decrease in emission at 603 nm with increasing temperature within the range of 120–260 K, while the emission at 951 nm exhibits a positive correlation within the same temperature range. This phenomenon suggests the potential use of the fluorescence intensity ratio (FIR) technique for precise temperature measurements. The relationship between temperature and FIR can be described by the following eqn (5):[45]

$$\mathrm{FIR} = \frac{I_{951}}{I_{603}} = \frac{I_{0.951}}{I_{0.603}} \frac{1 + A_{951}\exp(-\Delta E_{951}/K_B T)}{1 + A_{604}\exp(-\Delta E_{603}/K_B T)} \approx B + Ce^{-\Delta E/K_B T}, \quad (5)$$

where constants B, C and ΔE are related to the properties of Sb^{3+}/Sm^{3+}. Fig. 5d shows the relationship between FIR, calculated as $I_{603\ \mathrm{nm}}/I_{951\ \mathrm{nm}}$ and experimental temperature T. It is noted that when the temperature rises from 120 to 260 K, the FIR value increases from 0.06 to 0.2. In the field of tempera-

ture sensing, absolute temperature sensitivity (S_a) and relative temperature sensitivity (S_r) are crucial factors to consider when assessing an optical temperature measurement. The values of (S_a) and S_r can be calculated by eqn (6) and (7):[46,47]

$$S_a = \left|\frac{\partial \mathrm{FIR}}{\partial T}\right| = Ce^{-\Delta E/K_B T} \times \frac{\Delta E}{K_B T^2} \quad (6)$$

$$S_r = 100\% \times \left|\frac{1}{\mathrm{FIR}}\frac{\partial \mathrm{FIR}}{\partial T}\right| = 100\% \times \frac{Ce^{-\Delta E/K_B T}}{B + Ce^{-\Delta E/K_B T}} \times \frac{\Delta E}{K_B T^2} \quad (7)$$

As shown in Fig. 5e and f, for the samples, the maximum values of S_a and S_r are 0.14 and 1.08% K^{-1}, respectively. In addition to the high sensitivity, the repeatability and stability of optical temperature measurements are also critical. Among the same type of rare-earth doped perovskites, the S_a and S_r values of optical temperature measurements in this work are among leading values (Table S2†). Temperature resolution (δT) is another important parameter to evaluate the performance of optical thermometry, which can be expressed as follows:

$$\delta T = \frac{1}{S_r}\frac{\Delta \mathrm{FIR}}{\mathrm{FIR}} \quad (8)$$

In this case, ΔFIR/FIR stands for the relative error in the measurement process, and its value is approximately 0.5%.[47,48] Hence, it is calculated that the minimum temperature resolution is 0.46 at 160 K. At the same time, the non-contact optical thermometry of Sb^{3+}/Sm^{3+} co-doped Cs_2NaYCl_6 has a good repeatability. The above results indicate that Sb^{3+}/Sm^{3+} co-doped Cs_2NaYCl_6 is a potential material for non-contact optical thermometers. Additionally, Sb^{3+}:Cs_2NaYCl_6 and the Sb^{3+}/Sm^{3+} co-doped Cs_2NaYCl_6 double perovskites exhibit light emission under excitation by high-energy X-rays, as depicted in Fig. 5g. We conducted experiments at various X-ray power intensities to establish the relationship between emission and X-ray intensity. Notably, the radioluminescence (RL) intensity of Sb^{3+}/Sm^{3+} co-doped Cs_2NaYCl_6 displays a linear correlation with the power of X-rays, as illustrated in Fig. 5h and i.

3. Conclusions

In summary, the Sb^{3+}/Sm^{3+} co-doped Cs_2NaYCl_6 rare-earth double perovskites with a tunable emission and excellent stability were synthesized *via* a solvothermal method. It was found that the transition of $^3P_1 \rightarrow {}^1S_0$ could be split into two transitions due to the Jahn–Teller effect, resulting in a double STE emission within a temperature range of 80 to 260 K. However, as the temperature increases, the excited electrons tend to move toward a higher energy STE emission, leading to the disappearance of the low-energy STE emission within the same temperature range (80–260 K). By adjusting the Sm^{3+} feeding concentration, we were able to adjust the energy transfer efficiency between STE and Sm^{3+} emissions. Furthermore, the Sb^{3+}/Sm^{3+} co-doped Cs_2NaYCl_6 double perovskites exhibited multifunctional applications in high-energy X-rays and night vision. These double perovskites possess excellent optical properties and stability, rendering them promising candidates for applications in white-light illumination and temperature sensing.

Conflicts of interest

There are no conflicts to declare.

Acknowledgements

This work was supported by the National Natural Science Foundation of China (Grant No. 52162021 and 22175043), Open Foundation of State Key Laboratory of Featured Metal Materials and Life-cycle Safety for Composite Structures (Grant No. MMCS2023OF05), and Guangxi Science and Technology Plan Project (Guike AA23073018). The calculation was supported by the high-performance computing platform of Guangxi University.

References

1 Y. Bao, H. Wang, M. An, H. Tang, J. Li, J. Li, C. Tan, Y. Luo, J. Xu and Y. Yang, Defect-modulated synthesis and optoelectronic properties in chemical vapor deposited $CsPbBr_3$ microplates, *Nano Res.*, 2024, **17**, 4610–4615.
2 Y. Jiang, C. Sun, J. Xu, S. Li, M. Cui, X. Fu, Y. Liu, Y. Liu, H. Wan, K. Wei, T. Zhou, W. Zhang, Y. Yang, J. Yang, C. Qin, S. Gao, J. Pan, Y. Liu, S. Hoogland, E. H. Sargent, J. Chen and M. Yuan, Synthesis-on-substrate of quantum dot solids, *Nature*, 2022, **612**, 679–684.
3 M. Cui, C. Qin, Z. Zhou, Y. Jiang, S. Zhang, Z. Yuan, M. Yuan, K. Yu, Y. Jiang and Y. Liu, Tuning coherent phonon dynamics in two-dimensional phenylethylammonium lead bromide perovskites, *Nano Res.*, 2023, **16**, 3408–3414.
4 C. Zhao, C. Zhu, Y. Yu, W. Xue, X. Liu, F. Yuan, J. Dai, S. Wang, B. Jiao and Z. Wu, Multifunctional short-chain 2-thiophenealkylammonium bromide ligand-assisted perovskite quantum dots for efficient light-emitting diodes, *ACS Appl. Mater. Interfaces*, 2023, **15**, 40080–40087.
5 X. Hu, Y. Xu, J. Wang, J. Ma, L. Wang and W. Jiang, Ligand-modified synthesis of shape-controllable and highly luminescent $CsPbBr_3$ perovskite nanocrystals under ambient conditions, *Inorg. Chem. Front.*, 2022, **9**, 6080–6090.
6 Q. Lin, S. Bernardi, B. Shabbir, Q. Ou, M. Wang, W. Yin, S. Liu, A. S. R. Chesman, S. O. Fürer, G. Si, N. Medhekar, J. Jasieniak, A. Widmer-Cooper, W. Mao and U. Bach, Phase-control of single-crystalline inorganic halide perovskites via molecular coordination engineering, *Adv. Funct. Mater.*, 2022, **32**, 2109442.
7 Y. Xie, A. Zhou, X. Zhang, Q. Ou and S. Zhang, Metal cation substitution of halide perovskite nanocrystals, *Nano Res.*, 2022, **15**, 6522–6550.

8 R. Zeng, L. Zhang, Y. Xue, B. Ke, Z. Zhao, D. Huang, Q. Wei, W. Zhou and B. Zou, Highly efficient blue emission from self-trapped excitons in stable Sb^{3+}-doped $Cs_2NaInCl_6$ double perovskites, *J. Phys. Chem. Lett.*, 2020, **11**, 2053–2061.

9 Z. Xiao, K. Du, W. Meng, J. Wang, D. B. Mitzi and Y. Yan, Intrinsic instability of $Cs_2In(I)M(III)X_6$ (M = Bi, Sb; X = Halogen) double perovskites: a combined density functional theory and experimental study, *J. Am. Chem. Soc.*, 2017, **139**, 6054–6057.

10 D. Li, J. Song, Y. Cheng, X. Wu, Y. Wang, C. Sun, C. Yue and X. Lei, Ultra-sensitive, selective and repeatable fluorescence sensor for methanol based on a highly emissive 0D hybrid lead-free perovskite, *Angew. Chem., Int. Ed.*, 2022, **61**, e202206437.

11 Z. Chen, F. Zhang, D. Yang, H. Ji, X. Chen, D. Wu, X. Li, Y. Zhang and Z. Shi, Doping suppresses lattice distortion of vacant quadruple perovskites to activate self-trapped excitons emission, *Nano Res.*, 2024, **17**, 3068–3078.

12 S. Wu and Y. Liu, Recent advancements and manipulation strategies of colloidal $Cs_2BIBIIIX_6$ lead-free halide double perovskite nanocrystals, *Nano Res.*, 2023, **16**, 5572–5591.

13 H. Yang, X. Chen, Y. Chu, C. Sun, H. Lu, M. Yuan, Y. Zhang, G. Long, L. Zhang and X. Li, A universal hydrochloric acid-assistant powder-to-powder strategy for quick and mass preparation of lead-free perovskite microcrystals, *Light: Sci. Appl.*, 2023, **12**, 75.

14 C. Wang, J. Xiao, Z. Yan, X. Niu, T. Lin, Y. Zhou, J. Li and X. Han, Colloidal synthesis and phase transformation of all-inorganic bismuth halide perovskite nanoplates, *Nano Res.*, 2023, **16**, 1703–1711.

15 A. Huang, M. Liu, C. Duan, K. Wong and P. A. Tanner, Understanding the ultraviolet, green, red, near infrared and infrared emission properties of bismuth halide double perovskite, *Inorg. Chem. Front.*, 2022, **9**, 6379–6390.

16 J. Luo, X. Wang, S. Li, J. Liu, Y. Guo, G. Niu, L. Yao, Y. Fu, L. Gao, Q. Dong, C. Zhao, M. Leng, F. Ma, W. Liang, L. Wang, S. Jin, J. Han, L. Zhang, J. Etheridge, J. Wang, Y. Yan, E. H. Sargent and J. Tang, Efficient and stable emission of warm-white light from lead-free halide double perovskites, *Nature*, 2018, **563**, 541–545.

17 S. Bao, H. Yu, G. Gao, H. Zhu, D. Wang, P. Zhu and G. Wang, Rare-earth single atom based luminescent composite nanomaterials: tunable full-color single phosphor and applications in WLEDs, *Nano Res.*, 2022, **15**, 3594–3605.

18 Y. Chen, R. Zeng, Q. Wei, S. Zhang, B. Luo, C. Chen, X. Zhu, S. Cao, B. Zou and J. Z. Zhang, Competing energy transfer-modulated dual emission in Mn^{2+}-doped $Cs_2NaTbCl_6$ rare-earth double perovskites, *J. Phys. Chem. Lett.*, 2022, **13**, 8529–8536.

19 H. Wang, J. Yao, Q. Wei, J. Zhao, B. Zou and R. Zeng, Simultaneously achieving multicolor emission of down-shifting and up-conversion in Yb^{3+}, Er^{3+}-codoped $Cs_2NaGdCl_6$ double perovskites, *Adv. Opt. Mater.*, 2023, **11**, 2300694.

20 Y. Liu, F. Di Stasio, C. Bi, J. Zhang, Z. Xia, Z. Shi and L. Manna, Near-infrared light emitting metal halides: materials, mechanisms, and applications, *Adv. Mater.*, 2024, 2312482.

21 Y. Huang, Y. Pan, C. Peng, Y. Ding, H. Lian, L. Li and J. Lin, Orange/cyan emissive sensors of Sb^{3+} for probing water via reversible phase transformation in rare-earth-based perovskite crystals, *Inorg. Chem. Front.*, 2023, **10**, 991–1000.

22 Y. Hua, T. Wang, J. S. Yu, W. Ran and L. Li, Modulating A site compositions of europium(III)-doped double-perovskite niobate phosphors, *Inorg. Chem. Front.*, 2022, **9**, 6211–6224.

23 L. Zhang and M. Yuan, Lanthanide doped lead-free double perovskites as the promising next generation ultra-broadband light sources, *Light: Sci. Appl.*, 2022, **11**, 99.

24 Y. Wang, P. Dang, L. Qiu, G. Zhang, D. Liu, Y. Wei, H. Lian, G. Li, Z. Cheng and J. Lin, Multimode luminescence tailoring and improvement of $Cs_2NaHoCl_6$ cryolite crystals via Sb^{3+}/Yb^{3+} alloying for versatile photoelectric applications, *Angew. Chem., Int. Ed.*, 2023, **62**, e202311699.

25 Z. Rao, M. Cao, Z. Chen, X. Zhao and X. Gong, Understanding and effective tuning of red-to-green upconversion emission in Ho-based halide double perovskite microcrystals, *Adv. Funct. Mater.*, 2024, **34**, 2311568.

26 D. Chen, X. Zhang, J. Wei, L. Zhou, P. Chen, Q. Pang and J. Z. Zhang, Simultaneous enhancement of near infrared luminescence and stability of $Cs_2AgInCl_6$:Cr^{3+} double perovskite single crystals enabled by a Yb^{3+} dopant, *Inorg. Chem. Front.*, 2022, **9**, 4695–4704.

27 Y. Liu, X. Rong, M. Li, M. S. Molokeev, J. Zhao and Z. Xia, Incorporating rare-earth Terbium(III) ions into $Cs_2AgInCl_6$:Bi nanocrystals toward tunable photoluminescence, *Angew. Chem., Int. Ed.*, 2020, **59**, 11634–11640.

28 S. Li, Q. Hu, J. Luo, T. Jin, J. Liu, J. Li, Z. Tan, Y. Han, Z. Zheng, T. Zhai, H. Song, L. Gao, G. Niu and J. Tang, Self-Trapped Exciton to Dopant Energy Transfer in Rare Earth Doped Lead-Free Double Perovskite, *Adv. Opt. Mater.*, 2019, **7**, 1901098.

29 P. Zhu, S. Thapa, H. Zhu, S. Wheat, Y. Yue and D. Venugopal, Composition engineering of lead-free double perovskites towards efficient warm white light emission for health and well-being, *J. Alloys Compd.*, 2023, **960**, 170836.

30 X. Li, X. Shen, M. Lu, J. Wu, Y. Zhong, Z. Wu, W. W. Yu, Y. Gao, J. Hu, J. Zhu, Y. Zhang and X. Bai, Wide-coverage and efficient NIR emission from single-component nanophosphors through shaping multiple metal-halide packages, *Angew. Chem., Int. Ed.*, 2023, **62**, e202217832.

31 R. Tang, Y. Yang, Y. Yang, X. Ouyang, J. Che, S. Chen, X. Yao, B. Deng and R. Yu, A novel reddish-orange emitting $NaSrBiTeO_6$:Sm^{3+} phosphor with high moisture resistance and thermostability for horticultural light emitting diode applications, *J. Am. Ceram. Soc.*, 2024, **107**, 3012–3027.

32 S. K. Cushing, M. Li, F. Huang and N. Wu, Origin of strong excitation wavelength dependent fluorescence of graphene oxide, *ACS Nano*, 2014, **8**, 1002–1013.

33 J. Nie, H. Li, S. Fang, B. Zhou, Z. Liu, F. Chen, Y. Wang and Y. Shi, Efficient red photoluminescence in holmium-doped $Cs_2NaInCl_6$ double perovskite, *Cell Rep. Phys. Sci.*, 2022, **3**, 100820.

34 J. Li, Z. Tan, M. Hu, C. Chen, J. Luo, S. Li, L. Gao, Z. Xiao, G. Niu and J. Tang, Antimony doped Cs_2SnCl_6 with bright and stable emission, *Front. Optoelectron.*, 2019, **12**, 352–364.

35 Y. Jing, Y. Liu, M. Li and Z. Xia, Photoluminescence of singlet/triplet self-trapped excitons in Sb^{3+}-based metal halides, *Adv. Opt. Mater.*, 2021, **9**, 2002213.

36 H. Arfin, A. S. Kshirsagar, J. Kaur, B. Mondal, Z. Xia, S. Chakraborty and A. Nag, ns^2 electron (Bi^{3+} and Sb^{3+}) doping in lead-free metal halide perovskite derivatives, *Chem. Mater.*, 2020, **32**, 10255–10267.

37 Y. Jing, Y. Liu, X. Jiang, M. S. Molokeev, Z. Lin and Z. Xia, Sb^{3+} dopant and halogen substitution triggered highly efficient and tunable emission in lead-free metal halide single crystals, *Chem. Mater.*, 2020, **32**, 5327–5334.

38 A. Shinde, R. Gahlaut and S. Mahamuni, Low-temperature photoluminescence studies of $CsPbBr_3$ quantum dots, *J. Phys. Chem. C*, 2017, **121**, 14872–14878.

39 J. Ghosh, L. P. L. Mawlong, M. G. B, A. J. Pattison, W. Theis, S. Chakraborty and P. K. Giri, Solid-state synthesis of stable and color tunable cesium lead halide perovskite nanocrystals and the mechanism of high-performance photodetection in a monolayer $MoS_2/CsPbBr_3$ vertical heterojunction, *J. Mater. Chem. C*, 2020, **8**, 8917–8934.

40 Z. Tan, Y. Chu, J. Chen, J. Li, G. Ji, G. Niu, L. Gao, Z. Xiao and J. Tang, Lead-free perovskite variant solid solutions $Cs_2Sn_{1-x}Te_xCl_6$: bright luminescence and high anti-water stability, *Adv. Mater.*, 2020, **32**, 2002443.

41 D. Zhu, M. L. Zaffalon, J. Zito, F. Cova, F. Meinardi, L. De Trizio, I. Infante, S. Brovelli and L. Manna, Sb-doped metal halide nanocrystals: a 0D versus 3D comparison, *ACS Energy Lett.*, 2021, **6**, 2283–2292.

42 B. Zhou, Z. Liu, S. Fang, H. Zhong, B. Tian, Y. Wang, H. Li, H. Hu and Y. Shi, Efficient white photoluminescence from self-trapped excitons in Sb^{3+}/Bi^{3+}-codoped $Cs_2NaInCl_6$ double perovskites with tunable dual-emission, *ACS Energy Lett.*, 2021, **6**, 3343–3351.

43 W. Zhang, J. Wei, Z. Gong, P. Huang, J. Xu, R. Li, S. Yu, X. Cheng, W. Zheng and X. Chen, Unveiling the excited-state dynamics of Mn^{2+} in 0D Cs_4PbCl_6 perovskite nanocrystals, *Adv. Sci.*, 2020, **7**, 2002210.

44 T. Chang, H. Wang, Y. Gao, S. Cao, J. Zhao, B. Zou and R. Zeng, Component engineering to tailor the structure and optical properties of Sb-doped Indium-based halides, *Inorg. Chem.*, 2022, **61**, 1486–1494.

45 J. Xue, M. Song, H. M. Noh, S. H. Park, B. R. Lee, J. H. Kim and J. H. Jeong, Near-ultraviolet light induced red emission in Sm^{3+}-activated $NaSrLa(MoO_4)O_3$ phosphors for solid-state illumination, *J. Alloys Compd.*, 2020, **817**, 152705.

46 W. Li, S. Wu, H. Zhang, X. Zhang, J. Zhuang, C. Hu, Y. Liu, B. Lei, L. Ma and X. Wang, Enhanced biological photosynthetic efficiency using light-harvesting engineering with dual-emissive carbon dots, *Adv. Funct. Mater.*, 2018, **28**, 1804004.

47 X. Li, D. Wang, Y. Zhong, F. Jiang, D. Zhao, S. Sun, P. Lu, M. Lu, Z. Wang, Z. Wu, Y. Gao, Y. Zhang, W. W. Yu and X. Bai, Halide double perovskite nanocrystals doped with rare-earth ions for multifunctional applications, *Adv. Sci.*, 2023, **10**, 2207571.

48 A. Zhang, Z. Sun, M. Jia, Z. Fu, B. C. Choi, J. H. Jeong and S. H. Park, Sm^{3+}-doped niobate orange-red phosphors with a double-perovskite structure for plant cultivation and temperature sensing, *J. Alloys Compd.*, 2021, **889**, 161671.